ARTICLES
nature physics

| DOI: 10.1038/NPHYS4177

Oleoplaning droplets on lubricated surfaces

Dan Daniel[1], Jaakko V. I. Timonen[1,2], Ruoping Li[3], Seneca J. Velling[3] and Joanna Aizenberg[1,3,4]*

Recently, there has been much interest in using lubricated surfaces to achieve extreme liquid repellency: a foreign droplet immiscible with the underlying lubricant layer was shown to slide off at a small tilt angle <5°. This behaviour was hypothesized to arise from a thin lubricant overlayer film sandwiched between the droplet and solid substrate, but this has not been observed experimentally. Here, using thin-film interference, we are able to visualize the intercalated film under both static and dynamic conditions. We further demonstrate that for a moving droplet, the film thickness follows the Landau–Levich–Derjaguin law. The droplet is therefore oleoplaning—akin to tyres hydroplaning on a wet road—with minimal dissipative force and no contact line pinning. The techniques and insights presented in this study will inform future work on the fundamentals of wetting for lubricated surfaces and enable their rational design.

The ability to create materials with extreme liquid repellency has broad technological implications in areas ranging from drag reduction to prevention of icing and biofouling[1,2]. On a flat substrate, a droplet experiences significant pinning forces at the three-phase contact line[3–5]. To reduce contact line pinning, the conventional approach is to design micro/nanostructured surfaces that maintain a stable air layer within the structures, and hence minimize solid/liquid contact area (lotus effect)[2,6]. A liquid droplet sitting on such a surface beads up into a ball with a high apparent contact angle $\theta_{\mathrm{app}} > 150°$, and is able to roll off even at a small tilt angle θ_{tilt} with negligible contact angle hysteresis $\Delta\theta < 10°$ (Cassie–Baxter state). However, the solid/liquid contact cannot be completely removed with this approach, and the remaining contact points serve as nucleation/attachment sites for ice formation, solid and liquid contaminants, fouling organisms and biofilms[7,8]. Moreover, droplets can displace the air layer, penetrate into the structures and become highly pinned (Wenzel state)[9–11]; vapours can condense directly into the structures[12], and the micro/nanostructures also typically lack mechanical robustness required for practical applications[13,14].

As a solution to the above problems, lubricated surfaces consisting of micro/nanostructures filled with different oils have been proposed and demonstrated[15,16]. It has been postulated that an intercalated lubricant film (and hence no contact between the applied external liquid and the solid substrate) is responsible for the liquid-repellent, anti-icing and anti-fouling properties of these surfaces[17–20]. Previous studies, utilizing confocal fluorescence microscopy, were able to establish the presence of a lubricant overlayer 'cloaking' a droplet, as well as the stability of lubricant trapped within micropores and between microstructures[21,22]. However, they did not conclusively confirm the presence of a stable intercalated lubricant film that separates the liquid droplet from the raised features of the solid substrate. Here, we make use of thin-film interference effect instead to probe the static and dynamical states of the intercalated film at a resolution down to a few nanometres (compared with some hundreds of nanometres/several micrometres for confocal fluorescence microscopy). This technique also does not require the addition of a dye to the droplet or lubricant, which may affect the wetting properties of the liquids, and hence skew the results. Briefly, we raster scanned the surface simultaneously with two focused beams of monochromatic lights with wavelengths $\lambda_{1,2} = 458$ and 633 nm, and captured the reflected light through the pinhole of a confocal microscope; thus, only reflected light from the focal plane, that is, the interface of interest, was able to reach the photomultiplier tube of the microscope (Fig. 1a and see Supplementary Fig. 1 for a schematic of the set-up). This is crucial, because the weak refractive index contrast between solid, lubricant and droplet leads to a weak reflection signal that can be overwhelmed by stray light. In the presence of a thin lubricant film, the light reflected off the solid/lubricant and lubricant/droplet interfaces will then interfere with one another constructively or destructively to give bright or dark fringes, respectively. From the reflection intensities of the two wavelengths, the lubricant film profile can be deduced unambiguously (see Supplementary Figs 1–3 for details). This technique, known as dual-wavelength reflection interference contrast microscopy, has been used previously to study the thin air film beneath a droplet as it impacts a solid substrate, as well as the focal adhesions of cells, with nanometric resolution[23–26].

First, we studied the equilibrium state of the lubricating thin film under a static (non-moving) droplet of another liquid, and observed three different distinct lubrication states: L1–3. The first lubrication state (L1) corresponds to a stable lubricant film and was observed in the case of silicone oil of viscosity $\eta = 10$ cP, sandwiched between a 1 μl water droplet and a flat, transparent polymethylpentene (PMP) substrate (Fig. 1b). Without the droplet, the initial lubricant thickness h_{init}, as measured using white-light interferometry, was about 5 μm, but this was being continuously drained out due to capillary pressure. The film thickness eventually stabilized by van der Waals interactions, within the experimental time (15 min), to its equilibrium value of $h_{\mathrm{vdw}} = 25 \pm 5$ nm (Fig. 1c). Thus, we confirm that the hypothesized stable, continuous lubricating thin film can indeed exist (Fig. 2a).

However, this film can easily be destabilized, for example, by replacing the water droplet with 60 wt% aqueous sucrose solution (lubrication state L2). Silicone oil dewets under the sucrose solution and forms small lubricant pockets that are stable in time (Fig. 2b). In addition, a clear contact line becomes visible at the droplet base for L2 (Fig. 2b-1), which in contrast is missing in L1 (Fig. 2a-1). We note that despite the very different lubricant behaviour at

---

[1]John A. Paulson School of Engineering and Applied Sciences, Harvard University, Cambridge, Massachusetts 02138, USA. [2]Department of Applied Physics, Aalto University School of Science, Espoo FI-02150, Finland. [3]Wyss Institute for Biologically Inspired Engineering, Harvard University, Cambridge, Massachusetts 02138, USA. [4]Department of Chemistry and Chemical Biology, Harvard University, Cambridge, Massachusetts 02138, USA.
*e-mail: jaiz@seas.harvard.edu

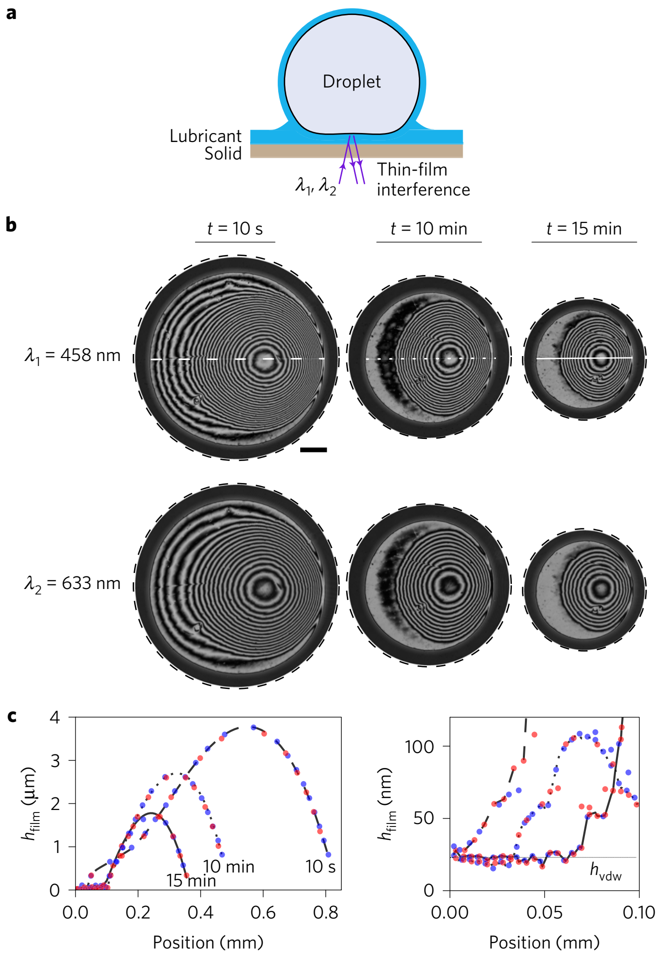

Figure 1 | Visualization of the lubricant film profile between the droplet and the solid using dual-wavelength, confocal reflection interference contrast microscopy. a, Schematic representing the thin-film interference effects due to the intercalated lubricant film. **b**, Fringes observed at wavelengths $\lambda_{1,2} = 458$ nm and 633 nm are due to a silicone oil film sandwiched between a water droplet and a flat PMP substrate at times $t = 10$ s, 10 min and 15 min after the droplet was deposited. Droplet size is decreasing due to evaporation. Scale bar, 0.1 mm. **c**, The corresponding film thickness profiles along the mid-section (lines in **b**) deduced using interference fringes at $\lambda_1 = 458$ nm and $\lambda_2 = 633$ nm (blue and red dots, respectively). The right panel is a magnified plot of the left panel for position = 0–0.1 mm, with a horizontal grey line to indicate the equilibrium film thickness $h_{\mathrm{vdw}} = 25 \pm 5$ nm.

the microscopic scale, droplets in the two lubrication states L1 and L2 still exhibit the same apparent macroscopic contact angle $\theta_{\mathrm{app}} = 90°$ and are thus practically impossible to distinguish using conventional contact angle instruments. Note that θ_{app} can be very different from the microscopic θ, which is obscured by the wetting ridge around the droplet but has been observed using confocal fluorescence microscopy[22]. In the third lubrication state (L3), lubricant is completely displaced under the droplet. This was the case for a dodecanol droplet on the same PMP substrate lubricated with silicone oil. The dodecanol droplet was irregularly shaped, highly pinned to the substrate with contact angle $\theta_{\mathrm{app}} = 23°$ (Fig. 2c). In addition to these examples, we looked at 23 other combinations of solid, lubricant oil, liquid and surface treatment, and found that all of them could be classified into these three lubrication categories (Supplementary Table 1).

We rationalize the lubrication states for different material combinations (solid, lubricant and liquid droplet) and surface treatments to originate from a combination of interfacial tensions effect and van der Waals interaction (Fig. 2d). The former is represented by the spreading constant $S = \gamma_{\mathrm{ls}} - (\gamma_{\mathrm{lo}} + \gamma_{\mathrm{os}})$, where γ_{ls}, γ_{lo} and γ_{os} are the liquid/solid, liquid/lubricant oil, lubricant oil/solid interfacial tensions, and the latter by the Hamaker constant A. For $S < 0$, S can be determined by measuring the contact angle of the droplet $\theta_{\mathrm{l}} < 180°$, while submerged inside the lubricant oil and using the relation $S = -\gamma_{\mathrm{lo}}\ (\cos\theta_{\mathrm{l}} + 1)$ (refs 17,27). When $\theta_{\mathrm{l}} = 180°$, $S \geq 0$. Earlier work has pointed out that for a lubricant film to be stable, $S > 0$ (refs 15,21). This, however, is not a sufficient condition, since $S > 0$ is the stability condition for a micrometre-thick film in the absence of other external destabilizing forces. A lubricant film beneath a droplet of radius R, on the other hand, is being continuously squeezed out with pressure $P \sim \gamma / R$ (Supplementary Fig. 4), and can be stabilized only if the disjoining pressure due to van der Waals interaction in the lubricant film $\Pi(h) = A/(6\pi h^3)$ is positive, that is, if $A > 0$ (refs 27,28). The coefficient A can be estimated by using the non-retarded Hamaker constant in Lifshitz theory:

$$A = \frac{3}{4} k_{\mathrm{B}} T \left(\frac{\epsilon_{\mathrm{o}} - \epsilon_{\mathrm{l}}}{\epsilon_{\mathrm{o}} + \epsilon_{\mathrm{l}}}\right) \left(\frac{\epsilon_{\mathrm{s}} - \epsilon_{\mathrm{o}}}{\epsilon_{\mathrm{s}} + \epsilon_{\mathrm{o}}}\right) + \frac{3\pi\hbar\nu_{\mathrm{e}}}{4\sqrt{2}} \times \frac{(n_{\mathrm{o}}^2 - n_{\mathrm{l}}^2)(n_{\mathrm{s}}^2 - n_{\mathrm{o}}^2)}{\sqrt{(n_{\mathrm{l}}^2 + n_{\mathrm{o}}^2)(n_{\mathrm{s}}^2 + n_{\mathrm{o}}^2)}\left[\sqrt{(n_{\mathrm{l}}^2 + n_{\mathrm{o}}^2)} + \sqrt{(n_{\mathrm{s}}^2 + n_{\mathrm{o}}^2)}\right]} \tag{1}$$

where $\nu_{\mathrm{e}} \approx 4 \times 10^{15}\ \mathrm{s}^{-1}$ is the plasma frequency of free-electron gas, k_{B} is the Boltzmann constant, T is the absolute temperature, $\hbar$ is the reduced Planck constant, while $\varepsilon_{\mathrm{l/o/s}}$ and $n_{\mathrm{l/o/s}}$ are the dielectric constants and refractive indices of the liquid droplet, oil lubricant and solid substrate, respectively[29].

Hence, for a stable, continuous lubricant layer, that is, lubrication state L1, two criteria must be met: $S > 0$ and $A > 0$. In all our schematics, the droplet is 'cloaked' by a lubricant layer, in which case $\gamma = \gamma_{\mathrm{lo}} + \gamma_{\mathrm{o}}$, where γ_{o} is the surface tension of oil; for a water droplet, this is usually the case, because water has a high surface tension, $\gamma_{\mathrm{l}} > \gamma_{\mathrm{lo}} + \gamma_{\mathrm{o}}$. It is possible, however, for the droplet not to be 'cloaked' when using a high-surface-energy lubricant, in which case $\gamma = \gamma_{\mathrm{l}}$ (refs 21,22). In any case, for typical material combinations, $\gamma \sim 50\ \mathrm{mN\,m^{-1}}$, whether or not there is cloaking, and $|A| \sim 10^{-21}$ J, and therefore at equilibrium, when $\Pi = P$, the equilibrium thickness $h_{\mathrm{vdw}} \sim (RA/\gamma)^{1/3}$ is about tens of nanometres, in agreement with our experimental observations (Fig. 1c). If the two criteria are not met, the lubricant film will dewet either partially (L2) or, in the extreme case when $S < -30\ \mathrm{mN\,m^{-1}}$, completely (L3), as summarized in the phase diagram of Fig. 2d. Note that the second term in equation (1) typically dominates since $\hbar\nu_{\mathrm{e}} \gg K_{\mathrm{B}}T$ at room temperature, and $A > 0$ when the optical properties of the lubricant oil, in particular its refractive index, are intermediate of those of the liquid droplet and the solid substrate, that is, $n_{\mathrm{s}} > n_{\mathrm{o}} > n_{\mathrm{l}}$ (equation (1))[27,29]. This is the case for stable silicone oil, $n_{\mathrm{o}} = 1.41$, sandwiched between a water droplet, $n_{\mathrm{l}} = 1.33$, and PMP substrate, $n_{\mathrm{s}} = 1.46$ (Fig. 2a), but not when the water droplet is replaced with a 60 wt% sucrose solution, $n_{\mathrm{l}} = 1.44$ (Fig. 2b). Hence, the silicone oil dewets into pockets under the sucrose droplet, even though $S > 0$. See Supplementary Figs 5 and 6 for details. Note that we have confined our discussion to the stability of the intercalated lubricant film beneath the droplet. Other possible wetting states, in particular those involving droplet 'cloaking' by a lubricant film, have been discussed in the literature[21,22].

Many lubricated surfaces reported previously have nano/microstructures on them to hold the lubricant oil in place for durability[15,16,19–21]. For a solid substrate with a hexagonal array of microposts, we observed three lubrication states SL1–3 for different solid/lubricant/droplet combinations (Fig. 3): there can be a stable, intercalated lubricant film (SL1), micrometre-sized

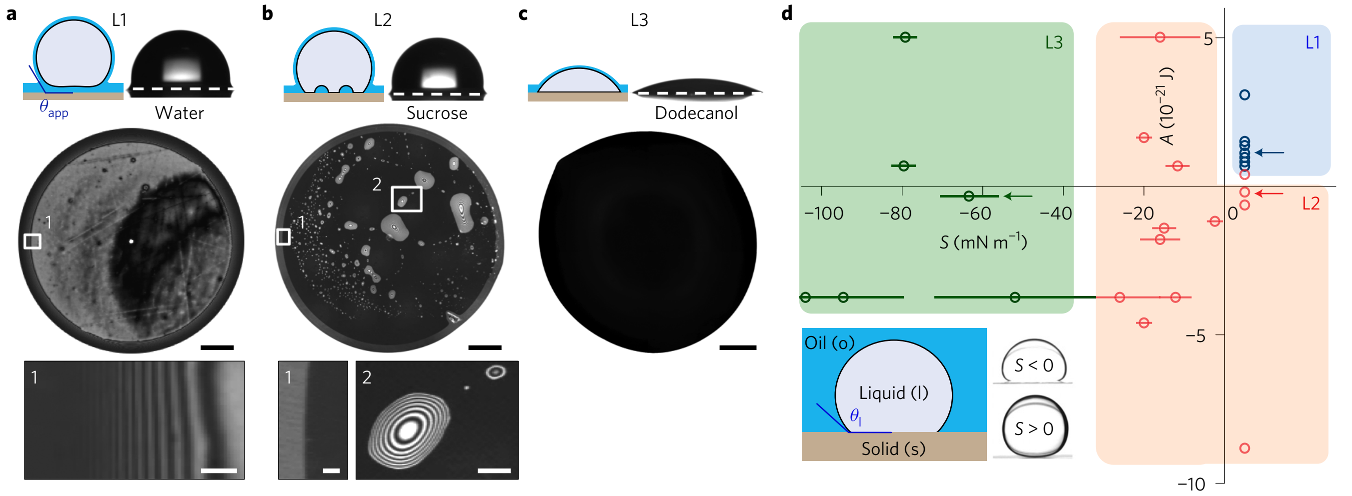

Figure 2 | Equilibrium lubrication states L1–3 of an oil film sandwiched between a droplet and a flat solid surface. **a**, L1: stable lubricant film (silicone oil) beneath a water droplet (0.1 mm scale bar, $\theta_{\mathrm{app}} = 90°$), with inset 1 (10 μm scale bar) showing the absence of a contact line. **b**, L2: lubricant film is unstable beneath 60 wt% sucrose solution and forms discrete pockets (0.3 mm scale bar, $\theta_{\mathrm{app}} = 90°$). Inset 1 (15 μm scale bar) shows the three-phase contact line, while inset 2 (40 μm scale bar) is a zoomed-in image of the lubricant pockets. **c**, L3: lubricant is completely displaced from beneath a dodecanol droplet (0.1 mm scale bar, $\theta_{\mathrm{app}} = 23°$). Solid substrate is PMP for **a**–**c**. **d**, Phase diagram of the lubrication states L1–3 (shaded blue, red and green, respectively) determined for 26 different combinations of substrate, lubricant oil, liquid and surface treatment. Data points corresponding to droplets in **a**–**c** are marked with arrows. $S = \gamma_{\mathrm{ls}} - (\gamma_{\mathrm{lo}} + \gamma_{\mathrm{os}})$ is the spreading constant that determines the stability of a micrometre-thick film; A is the Hamaker constant that determines the stability of a nanoscale film. Error bars in S come from uncertainty in measuring θ_l. See Supplementary Table 1 for the data used to generate the phase diagram.

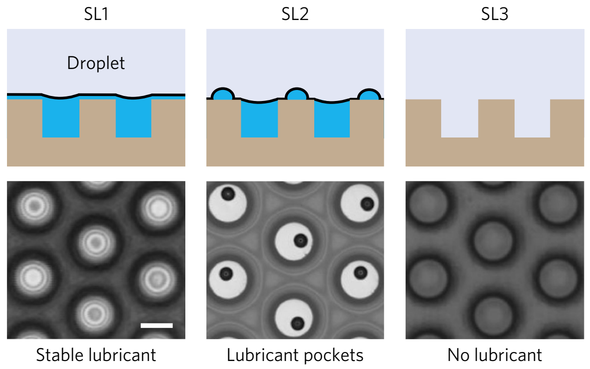

Figure 3 | Lubrication states for lubricant-infused surfaces bearing a hexagonal array of microposts with diameter $D = 26$ μm, pitch $p = 50$ μm and height $h_{\mathrm{p}} = 30$ μm. The liquid droplet is water, while the solid substrate is made from ultraviolet-cured polymer (NOA 61, Norland), lubricated with perfluorinated oil. Different wetting states are achieved by different surface treatment: SL1, 200 nm fluoropolymer coating; SL2, vapour-phase silanization with perfluorosilane; SL3, no surface treatment. See Methods for details on sample preparation. Scale bar, 25 μm.

lubricant pockets on top of posts (SL2), or complete displacement of lubricant under static conditions (see Supplementary Section 4 and Supplementary Movies 1 and 2).

While we have discussed the lubrication states under static conditions, we also observed very different lubricant dynamics under motion; for example, for moving droplets in L1 and L2—where, under static conditions, there is a stable nanometric and partially dewetted film, respectively—micrometre-thick lubricant film was instead observed; that is, the droplet is oleoplaning when mobilized (see Supplementary Fig. 7 for the wetting–dewetting transitions of a droplet in L2). The thickness of this film increases with increasing velocity and follows the Landau–Levich–Derjaguin (LLD) law; this is analogous to liquid films entrained during the dip-coating process and the bubble rise in a capillary tube[27,30–33]. At the rim around the droplet base of size l, there is a capillary pressure-driven flow (see the schematics in Fig. 4a). The film thickness h_{film} can thus be predicted by balancing ∇P and $\eta \nabla^2 U$ in this region, that is, $\gamma_{\mathrm{lo}}/Rl \sim \eta U/h^2$, and matching the curvature in this transition region, $\partial^2 h/\partial x^2 \sim h_{\mathrm{film}}/l^2$, with that of the main droplet, $1/R$, that is, $h_{\mathrm{film}}/l^2 \sim 1/R$. This gives

$$l \sim R\,\mathrm{Ca}^{1/3}$$

$$h_{\mathrm{film}} = h_{\mathrm{LLD}} \sim R\,\mathrm{Ca}^{2/3} \tag{2}$$

where $\mathrm{Ca} = \eta U/\gamma_{\mathrm{lo}}$ is the capillary number (see Supplementary Fig. 8). For a typical $\mathrm{Ca} = 10^{-4}$, $h \ll l \ll R$, and hence justifies the use of lubrication approximation in this analysis.

Experimentally, we found that the LLD law was well obeyed for a droplet of volumes $V = 5$–10 μl moving at speeds $U = 0.05$–0.6 mm s^{-1} on fluoropolymer-coated, flat substrate infused with perfluorinated oil with $\eta = 30$–60 cP (filled circles, Fig. 4a). We measured h_{film} using white-light interferometry: a white light was shone from beneath a moving droplet and its reflected signal was captured by an optical fibre into a spectrometer. Depending on the wavelength of the light, there can be either constructive or destructive interferences, resulting in characteristic oscillations of the reflected intensity I with λ (See schematic in Fig. 4a and Supplementary Figs 9 and 10). From these oscillations, the thickness of h_{film} along the mid-section of the droplet—where it is flattest—can be determined with an accuracy of $\Delta h_{\mathrm{film}} < 0.2$ μm. Figure 4b shows an interferogram of a 1 μl water droplet oleoplaning at $U = 0.4$ mm s^{-1} over a lubricant film (perfluorinated oil, $\eta = 30$ cP) of thickness $h_{\mathrm{film}} = h_{\mathrm{LLD}}$. For the same substrate decorated with microposts of height h_{p}, $h_{\mathrm{film}} = h_{\mathrm{LLD}}$, as long as $h_{\mathrm{LLD}} > h_{\mathrm{p}}$ (Fig. 4c and open circles, Fig. 4a). However, if $h_{\mathrm{p}} > h_{\mathrm{LLD}}$, h_{film} is then set by h_{p}, that is, $h_{\mathrm{film}} = h_{\mathrm{p}}$ with only a submicrometre, intercalated lubricant film between the droplet and the top of the posts (Fig. 4d and open squares, Fig. 4a). See Supplementary Movies 3 and 4 for droplets oleoplaning on micropost surfaces with $h_{\mathrm{p}} = 2$ μm and 10 μm, respectively.

To characterize the differences in droplet mobility between the two oleoplaning states, that is, when $h_{\mathrm{film}} = h_{\mathrm{LLD}}$ and $h_{\mathrm{film}} = h_{\mathrm{p}}$,

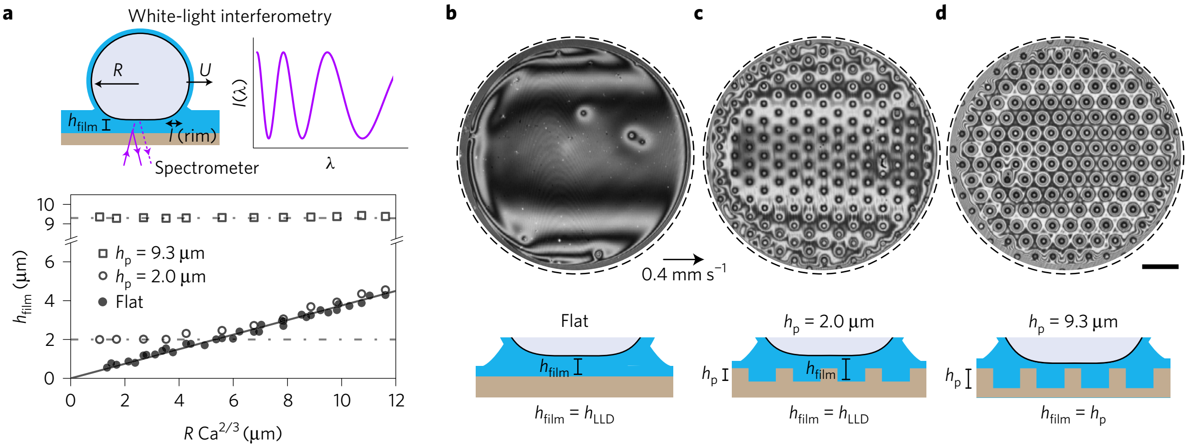

Figure 4 | Micrometre-thick lubricant film stabilized under motion. a, The film thickness in the middle region of water droplets ($V = 5$–$10\,\mu$l) moving at controlled speed $U = 0.05$–$0.6\,\mathrm{mm\,s^{-1}}$ is measured using white-light interferometry. The thickness predicted by the LLD law, $h_{LLD} \sim R\,\mathrm{Ca}^{2/3}$, is shown by the full line, where R is the droplet radius, and $\mathrm{Ca} = \eta U/\gamma_{lo}$ is the capillary number. For most data points, there are three repeats, with a standard deviation of $0.2\,\mu$m. **b**, For a flat substrate, a $1\,\mu$l water droplet moving at $U = 0.4\,\mathrm{mm\,s^{-1}}$ oleoplanes over a lubricant film, whose thickness is determined by the LLD law, $h_{film} = h_{LLD}$. **c**, The same law applies for a micropost surface with post height, $h_p = 2\,\mu\mathrm{m} < h_{LLD}$. **d**, In contrast, when $h_p = 10\,\mu$m, $h_{film} = h_p$ with only a submicrometre, intercalated lubricant film between the droplet and the top of the posts. For **b–d**, the interferograms are taken at $\lambda_2 = 633$ nm and the scale bar is 0.1 mm.

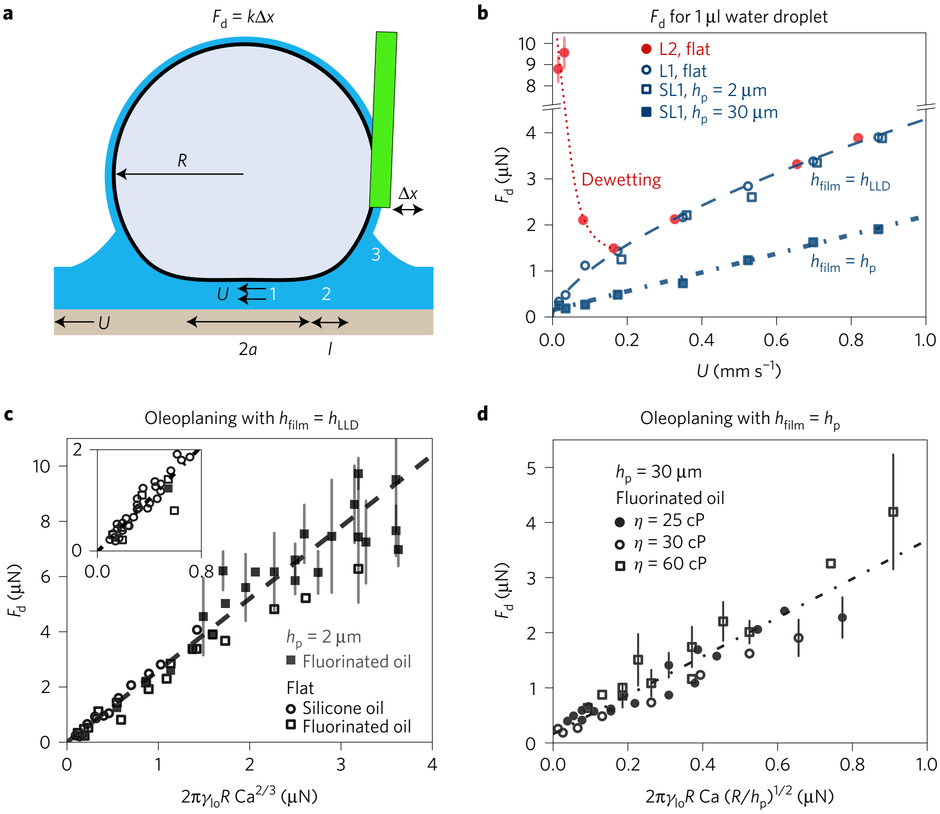

Figure 5 | Dissipative force F_d acting on oleoplaning droplets. a, Schematic of the cantilever force sensor to measure F_d. **b**, Plot shows F_d acting on $1\,\mu$l water droplets moving on flat, lubricated substrates (lubrication states L1 and L2), as well as lubricated, micropost surfaces ($h_p = 30\,\mu$m). The lubricant is perfluorinated oil with $\eta = 30$ cP. **c**, When oleoplaning with $h_{film} = h_{LLD}$, F_d follows equation (3) for water droplets of volumes $V = 1$–$5\,\mu$l, oleoplaning over silicone oil and fluorinated oil of different viscosities, $\eta = 5$–60 cP. **d**, In contrast, when $h_{film} = h_p$, F_d follows equation (4). For **b–d**, each data point is repeated at least three times, with a standard deviation, $\Delta F_d < 0.3\,\mu$N, unless otherwise indicated by the error bars.

we built a customized cantilever force sensor and measured the dissipative force F_d acting on a moving droplet with a sensitivity of about $0.1\,\mu$N (Fig. 5a). Similar set-ups have been reported elsewhere[34–36]. Briefly, the droplet was attached by its own capillarity to an acrylic tube with inner and outer radii of 0.29 and 0.36 mm, respectively, while the substrate was moved at a controlled speed U in the range of 0.01–$1\,\mathrm{mm\,s^{-1}}$ (see Supplementary Figs 11 and 12 for details of the set-up). F_d can then be inferred from the deflection of the capillary tube Δx, since $F_d = k\Delta x$, where $k = 6$–$30\,\mathrm{mN\,m^{-1}}$ for tube lengths $L = 6$–10 cm.

We observed that F_d increases monotonically with U for oleoplaning droplets, with $F_d \propto U^{2/3}$ and $\propto U$ for $h_{film} = h_{LLD}$ and

$h_{\mathrm{film}} = h_{\mathrm{p}}$, respectively (Fig. 5b). Note that for lubrication states L1 and SL1, we observed no pinning of the droplet even at the lowest experimentally realizable velocity of $10\,\mu\mathrm{m\,s^{-1}}$, and $F_{\mathrm{d}} \to 0$ as $U \to 0$. We attribute this behaviour to the stable lubricant layer that prevents pinning and gives rise to velocity-dependent, viscous dissipative force. For lubrication state L2, the droplet is also oleoplaning when $U > 0.2\,\mathrm{mm\,s^{-1}}$, and $F_{\mathrm{d}}(U)$ for $U > 0.2\,\mathrm{mm\,s^{-1}}$ is indistinguishable between L1 and L2 for the same droplet ($1\,\mu\mathrm{l}$ water droplet) and lubricant (perfluorinated oil, $\eta = 30\,\mathrm{cP}$). This also explains why droplets in L2 remain mobile and have low θ_{tilt} (see Supplementary Movie 5). However, at lower velocity, the lubricant film dewets and the droplet becomes pinned, with $F_{\mathrm{d}} = 9 \pm 1\,\mu\mathrm{N}$ as $U \to 0$ (see Supplementary Fig. 7 for interferograms showing the wetting–dewetting transition).

The functional form of the dissipative force F_{d} for oleoplaning droplets can be derived as follows. First, we note that the lubricant is more viscous than the droplet in our experiments, and thus the droplet rolls while oleoplaning. This can be confirmed by seeding the droplet with tracer particles (see Supplementary Fig. 13). Beneath the droplet (region 1, Fig. 5a), there is therefore plug flow of the lubricant (in the reference frame of the droplet), that is, $\nabla_z U = 0$, and hence minimal viscous dissipation. Most of the viscous dissipation occurs instead at the small transition region 2 of size l at the rim of region 1, where there is a capillary pressure-driven flow, as discussed previously. The dissipative force F_{d} can then be estimated by integrating the viscous stress $\eta U/h$ over the area $2\pi a l \approx 2\pi R l$ (the fact that $a \sim R$ is experimentally verified in Supplementary Fig. 14). For a Landau–Levich film, where $h_{\mathrm{film}} = h_{\mathrm{LLD}} \sim R\,\mathrm{Ca}^{2/3}$ and $l \sim R\,\mathrm{Ca}^{1/3}$, this gives

$$F_{\mathrm{d}} \approx (\eta U/h) 2\pi a l \approx 2\pi \gamma_{\mathrm{lo}} R\,\mathrm{Ca}^{2/3} \tag{3}$$

This scaling of F_{d} was confirmed experimentally, with a prefactor of 2.6, for $V = 1$–$5\,\mu\mathrm{l}$ water droplets moving at $U = 0.01$–$5\,\mathrm{mm\,s^{-1}}$ on PMP substrate lubricated with silicone oil of $\eta = 5$–$20\,\mathrm{cP}$, as well as on fluoropolymer-coated glass lubricated with perfluorinated oil of $\eta = 30$–$60\,\mathrm{cP}$ (Fig. 5c). Note that the presence of microposts (diameter $D = 18\,\mu\mathrm{m}$, pitch $p = 50\,\mu\mathrm{m}$) of $h_{\mathrm{p}} = 2\,\mu\mathrm{m} < h_{\mathrm{LLD}}$ does not change the scaling of F_{d}, although ΔF_{d} is larger and is probably due to defects/roughness on the microposts.

For micropost surfaces with taller $h_{\mathrm{p}} > h_{\mathrm{LLD}}$, h_{film} is equal to h_{p}. Assuming further that $h_{\mathrm{p}}/l^2 \sim 1/R$, F_{d} is now given instead by

$$F_{\mathrm{d}} \approx (\eta U/h_{\mathrm{p}}) 2\pi a l \approx 2\pi \gamma_{\mathrm{lo}} R\,\mathrm{Ca}\,(R/h_{\mathrm{p}})^{1/2} \tag{4}$$

This scaling was confirmed experimentally, with a prefactor of 3.5, for $V = 0.5$–$3\,\mu\mathrm{l}$ water droplets moving at $U = 0.01$–$1\,\mathrm{mm\,s^{-1}}$ on surfaces with $h_{\mathrm{p}} = 30\,\mu\mathrm{m}$ and different perfluorinated oils of different viscosities $\eta = 25$–$60\,\mathrm{cP}$ (Fig. 5d).

Despite the approximation of the three-dimensional lubricant flow as a two-dimensional Hele-Shaw flow, we have nevertheless captured the main physics of viscous dissipation in oleoplaning droplets; this simplification also probably accounts for the prefactors of 2.6 and 3.5 in equations (3) and (4), respectively. We also note that the predicted scaling of F_{d} is independent of the initial lubricant film thickness, $h_{\mathrm{init}} \neq h_{\mathrm{film}}$, or the size of the wetting ridge (region 3, Fig. 5a), which we also observed experimentally (Supplementary Fig. 15).

For oleoplaning droplets on lubricated surfaces, there is no three-phase contact line and hence the conventional concepts in contact line pinning, such as the Joanny–de Gennes model or molecular kinetic theory, no longer apply[3,5,37]; similarly, the contact angle hysteresis is ill-defined for oleoplaning droplets. Finally, we would like to add that the discussions above are valid only when droplets oleoplane over a continuous lubricant layer; should there be any dewetting, even if only partially, F_{d} becomes dominated by contact line pinning, and the scaling laws in equations (3) and (4) no longer hold true. See discussions in Supplementary Fig. 16.

In summary, we have observed and explained the main static and dynamic wetting states on lubricated surfaces. In addition to having a direct relevance to practical applications such as condensers, phase-change heat exchangers and water harvesting devices that largely rely on the droplet mobility, our results may have wide implications beyond the motion of droplets on lubricated surfaces: stabilization of the lubricant thin film is crucial, for example, to prevent adhesion of ice, biomolecules and living microorganisms or reduce drag on lubricated surfaces.

Methods

Methods, including statements of data availability and any associated accession codes and references, are available in the online version of this paper.

Received 16 August 2016; accepted 16 May 2017;

References

1. Bocquet, L. & Lauga, E. A smooth future? *Nat. Mat.* **10,** 334–337 (2011).
2. Quéré, D. Wetting and roughness. *Annu. Rev. Mater. Res.* **38,** 71–99 (2008).
3. Snoeijer, J. H. & Andreotti, B. Moving contact lines: scales, regimes, and dynamical transitions. *Annu. Rev. Fluid Mech.* **45,** 269–292 (2013).
4. Eral, H. B., 't Mannetje, D. J. C. M. & Oh, J. M. Contact angle hysteresis: a review of fundamentals and applications. *Colloid Polym. Sci.* **291,** 247–260 (2012).
5. Blake, T. D. The physics of moving wetting lines. *J. Colloid Interface Sci.* **299,** 1–13 (2006).
6. Reyssat, M., Richard, D., Clanet, C. & Quéré, D. Dynamical superhydrophobicity. *Faraday Discuss.* **146,** 19–33 (2010).
7. Sojoudi, H., Wang, M., Boscher, N., McKinley, G. & Gleason, K. Durable and scalable icephobic surfaces: similarities and distinctions from superhydrophobic surfaces. *Soft Matter* **12,** 1938–1963 (2016).
8. Genzer, J. & Efimenko, K. Recent developments in superhydrophobic surfaces and their relevance to marine fouling: a review. *Biofouling* **22,** 339–360 (2006).
9. Lafuma, A. & Quéré, D. Superhydrophobic states. *Nat. Mater.* **2,** 457–460 (2003).
10. Reyssat, M., Pépin, A., Marty, F., Chen, Y. & Quéré, D. Bouncing transitions on microtextured materials. *Europhys. Lett.* **74,** 306–312 (2006).
11. Tuteja, A., Choi, W., Mabry, J. M., McKinley, G. H. & Cohen, R. E. Robust omniphobic surfaces. *Proc. Natl Acad. Sci. USA* **105,** 18200–18205 (2008).
12. Dorrer, C. & Rühe, J. Condensation and wetting transitions on microstructured ultrahydrophobic surfaces. *Langmuir* **23,** 3820–3824 (2007).
13. Verho, T. *et al*. Mechanically durable superhydrophobic surfaces. *Adv. Mater.* **23,** 673–678 (2011).
14. Tian, X., Verho, T. & Ras, R. H. Moving superhydrophobic surfaces toward real-world applications. *Science* **352,** 142–143 (2016).
15. Lafuma, A. & Quéré, D. Slippery pre-suffused surfaces. *Europhys. Lett.* **96,** 56001 (2011).
16. Wong, T.-S. *et al*. Bioinspired self-repairing slippery surfaces with pressure-stable omniphobicity. *Nature* **477,** 443–447 (2011).
17. Baker, H. R., Bascom, W. D. & Singleterry, C. R. The adhesion of ice to lubricated surfaces. *J. Colloid Sci.* **17,** 477–491 (1962).
18. Grinthal, A. & Aizenberg, J. Mobile interfaces: liquids as a perfect structural material for multifunctional, antifouling surfaces. *Chem. Mater.* **26,** 698–708 (2014).
19. Kim, P. *et al*. Liquid-infused nanostructured surfaces with extreme anti-ice and anti-frost performance. *ACS Nano* **6,** 6569–6577 (2012).
20. Epstein, A. K., Wong, T.-S., Belisle, R. A., Boggs, E. M. & Aizenberg, J. Liquid-infused structured surfaces with exceptional anti-biofouling performance. *Proc. Natl Acad. Sci. USA* **109,** 13182–13187 (2012).
21. Smith, J. D. *et al*. Droplet mobility on lubricant-impregnated surfaces. *Soft Matter* **9,** 1772–1780 (2013).
22. Schellenberger, F. *et al*. Direct observation of drops on slippery lubricant-infused surfaces. *Soft Matter* **11,** 7617–7626 (2015).
23. de Ruiter, J., Mugele, F. & van den Ende, D. Air cushioning in droplet impact. I. Dynamics of thin films studied by dual wavelength reflection interference microscopy. *Phys. Fluids* **27,** 012104 (2015).
24. Curtis, A. S. G. The mechanism of adhesion of cells to glass. A study by interference reflection microscopy. *J. Cell. Biol.* **20,** 199–215 (1964).

25. Schilling, J., Sengupta, K., Goennenwein, S., Bausch, A. R. & Sackmann, E. Absolute interfacial distance measurements by dual-wavelength reflection interference contrast microscopy. *Phys. Rev. E* **69,** 021901 (2004).
26. Limozin, L. & Sengupta, K. Quantitative reflection interference contrast microscopy (RICM) in soft matter and cell adhesion. *Chem. Phys. Chem.* **10,** 2752–2768 (2009).
27. de Gennes, P.-G., Brochard-Wyart, F. & Quéré, D. *Capillarity and Wetting Phenomena: Drops, Bubbles, Pearls, Waves* (Springer Science & Business Media, 2013).
28. Brochard-Wyart, F., Di Meglio, J. M., Quéré, D. & de Gennes, P. G. Spreading of nonvolatile liquids in a continuum picture. *Langmuir* **7,** 335–338 (1991).
29. Israelachvili, J. N. *Intermolecular and Surface Forces* 3rd edn (Academic, 2011).
30. Landau, L. & Levich, V. Dragging of a liquid by a moving plate. *Acta Physicochim. USSR* **17,** 42–54 (1942).
31. Derjaguin, B. Thickness of liquid layer adhering to walls of vessels on their emptying and the theory of photo and motion-picture film coating. *Dokl. Acad. Sci. USSR* **39,** 13–16 (1943).
32. Bretherton, F. The motion of long bubbles in tubes. *J. Fluid Mech.* **10,** 166–188 (1961).
33. Cantat, I. Liquid meniscus friction on a wet plate: bubbles, lamellae, and foams. *Phys. Fluids* **25,** 031303 (2013).
34. Pilat, D. *et al*. Dynamic measurement of the force required to move a liquid drop on a solid surface. *Langmuir* **28,** 16812–16820 (2012).
35. Lagubeau, G., Le Merrer, M., Clanet, C. & Quéré, D. Leidenfrost on a ratchet. *Nat. Phys.* **7,** 395–398 (2011).
36. ‘t Mannetje, D. *et al*. Electrically tunable wetting defects characterized by a simple capillary force sensor. *Langmuir* **29,** 9944–9949 (2013).
37. Joanny, J. F. & de Gennes, P.-G. A model for contact angle hysteresis. *J. Chem. Phys.* **81,** 552–562 (1984).

Acknowledgements

We thank K.-C. Park, C. N. Kaplan and H. A. Stone for fruitful discussions. The work was supported by the Office of Naval Research, US Department of Defense, under MURI Award No. N00014-12-1-0875. J.V.I.T. was supported by the European Commission through the Seventh Framework Programme (FP7) project DynaSLIPS (project number 626954). We acknowledge the use of the facilities at the Harvard Center for Nanoscale Systems supported by the NSF under Award No. ECS-0335765 and at the Harvard Materials Research Science and Engineering Center (MRSEC) under Award No. DMR-1420570.

Author contributions

D.D., J.V.I.T. and J.A. conceived of and planned the experiments. D.D., R.L. and S.J.V. executed the experimental work. D.D., J.V.I.T. and J.A. analysed the experimental results and wrote the manuscript. All authors reviewed the manuscript.

Additional information

Supplementary information is available in the online version of the paper. Reprints and permissions information is available online at www.nature.com/reprints. Publisher’s note: Springer Nature remains neutral with regard to jurisdictional claims in published maps and institutional affiliations. Correspondence and requests for materials should be addressed to J.A.

Competing financial interests

J.A. is the founder of SLIPS Technologies, Inc.

Methods

Material and sample preparation. The plastic substrates (polymethylmethacrylate, polymethylpentene, polyimide, polypropene) were used as received without further modification. Organic contaminants on glass were removed using a piranha etch, by submerging it in a mixture of H_2SO_4/H_2O_2 (3:1) at 120 °C for 30 min, rendering the glass hydrophilic. It can then be made hydrophobic by vapour-phase silanization with dodecyltrichlorosilane (Gelest) or tridecafluorotrichlorosilane (Gelest) for 2 h. Alternatively, the hydrophobicity of glass can be tuned by flowing C_4F_8 under vacuum and RF plasma for different times (1–8 s; ref. 38). The resulting fluoropolymer-like coating is 5–10 nm thick (measured using ellipsometry). A much thicker fluoropolymer layer up to 200 nm can be deposited this way by increasing flow time to 15 min. The micropost surfaces were made from silicon masters through the replica moulding method, using ultraviolet-cured NOA 61 polymer[39]. The microposts were then made hydrophobic by either vapour-phase silanization or RF plasma sputtering as described previously. The thickness of the lubricant film was controlled by spin-coating and was kept at 3 μm thickness for a flat substrate. For micropost surfaces, the lubricant covers the posts completely with a lubricant overlayer of 1 μm, measured using white-light interferometry. The dissipative force acting on the droplet is however quite insensitive to exact lubricant film thickness.

Confocal reflection interference contrast microscopy. The interferograms were taken with either Leica TCS SP5 confocal microscopy or a Zeiss LSM 710 confocal microscope. The light path of the set-up and the details of the technique can be found in Supplementary Figs 1–3.

White-light interferometry. The optical fibre/reflection probe (R400-7-UV-VIS) and spectrometer were purchased from Ocean Optics. Details of the technique can be found in Supplementary Figs 9 and 10.

Data availability. The data that support the plots within this paper and other findings of this study are available from the corresponding author on reasonable request.

References

38. Bodas, D. S., Mandale, A. & Gangal, S. Deposition of PTFE thin films by RF plasma sputtering on ⟨100⟩ silicon substrates. *Appl. Surf. Sci.* **245,** 202 (2005).
39. Pokroy, B., Epstein, A. K., Persson-Gulda, M. & Aizenberg, J. Fabrication of bioinspired actuated nanostructures with arbitrary geometry and stiffness. *Adv. Mater.* **21,** 463–469 (2009).